Journal of the Mechanics and Physics of Solids 122 (2019) 126–140

Contents lists available at ScienceDirect

Journal of the Mechanics and Physics of Solids

journal homepage: www.elsevier.com/locate/jmps

The generalized Tabor parameter for adhesive rough contacts near complete contact

Michele Ciavarella[a], Yang Xu[b], Robert L. Jackson[b,*]

[a] Politecnico di BARI, Center of Excellence in Computational Mechanics, Viale Gentile 182, Bari, 70126, Italy
[b] Mechanical Engineering Department, Auburn University, Auburn, AL 36849, USA

ARTICLE INFO

Article history:
Received 30 November 2017
Revised 24 July 2018
Accepted 13 August 2018
Available online 25 August 2018

Keywords:
Roughness
Adhesion
Hysteresis
Gaussian distribution

ABSTRACT

Recently, the first author has obtained a model for adhesive contact near full contact under the JKR assumptions. The model shows, in the common case of low fractal dimensions, an 'unbounded' adhesion enhancement when larger and larger upper "truncation wavenumber" is considered in the spectrum of roughness, i.e. when we increase "magnification". Here, using a more general Maugis–Dugdale model, we show that a generalized multiscale Tabor parameter can be defined which shows a transition to a non-hysteretic regime, dependent on the root-mean-square (rms) slope of the surface. The contact area returns in the "fractal limit" to the adhesionless one. Two examples of rough surfaces from the literature are considered to show the full dependence on magnification of the adhesive solution. The choice of the truncation of the spectrum remains fundamentally arbitrary.

1. Introduction

Adhesion between randomly rough elastic bodies is a complicated problem, despite the main conclusion of experiments (Fuller and Tabor, 1975) is that amplitude of roughness is the primary parameter dominating the problem. As we realize that surface roughness is multiscale, many physical quantities seem to depend (according to some models) on short wavelength cutoffs determining slopes, curvatures and even higher order spectral moments, which are quantities not converging if one includes more and more details and scales of roughness. At the AFM scale, for instance, one may also find that slopes are so high that assumptions of linear elasticity, of infinitesimal deformation and rotations, of pressure being less than theoretical strength and many other assumptions are violated, so that one looses control of the model.

Recently, Pastewka and Robbins (2014) made an attempt of a fully numerical investigation of pull-off for a reasonably "multiscale" self-affine rough surface (still limited by computational capabilities to less than 3 orders of magnitude in wavelengths from the nano/atomic to the microscale wavelength) and concluded that pull-off data decay (Fig. S3 of their Suppl.Inf.) did not correlate well with classical (Fuller and Tabor, 1975) asperity model predictions, namely, the pull-off data are much higher. Pastewka and Robbins (2014) own attempt to define a stickiness parameter (based on the slope of the area-load curve) involves only rms slope and rms curvature, and this was suggested in strong contrast with asperity models whose emphasis is on the rms roughness height.

Persson (2002) tries to solve the multiscale problem in the JKR regime (after Johnson et al., 1971) who solved the case of the single elastic sphere) but seems to deal with only the loading regime, and

* Corresponding author.
E-mail addresses: Mciava@poliba.it (M. Ciavarella), jacksr7@auburn.edu (R.L. Jackson).

https://doi.org/10.1016/j.jmps.2018.08.011
0022-5096/

Persson and Scaraggi (2014), instead, aim at the non-hysteretic DMT regime (from Derjaguin–Muller–Toporov (DMT) solution of the sphere Derjaguin et al., 1975), and it is not clear when one can switch from one solution to the other (Johnson and Greenwood, 1997). Indeed, the original Tabor parameter (Tabor, 1977) only controls the validity of the DMT vs JKR regime for the sphere, and is

$$\mu_T = \left(\frac{Rw^2}{E^{*2}\Delta r^3}\right)^{1/3} = \frac{\left(Rl_a^2\right)^{1/3}}{\Delta r} = \frac{\sigma_0}{E^*}\left(\frac{R}{l_a}\right)^{1/3} \to 0, \tag{1}$$

where R is the sphere radius, w is work of adhesion, Δr is the range of attraction of adhesive forces, close to atomic distance, and E^* the plane strain elastic modulus. Also, σ_0 is the theoretical strength of the material, and we have introduced the length $l_a = w/E^*$ as an alternative measure of adhesion — for Lennard–Jones potential of elastic crystals, $l_a \simeq 0.05a_0$, where a_0 is the equilibrium distance and of the order of few tens of angstroms. Persson and Scaraggi (2014) attempt a generalization of the Tabor parameter, but it is mainly based on an empirical estimate of the relevant radius from truncation of the roughness.

In the present paper, we shall instead study rigorously the conditions of closing gaps near full contact, using a pressurized crack model, further elaborating on the concept introduced by XJM (Xu et al., 2014) who extended the idea of pressurized gaps which (Johnson et al., 1985) used for the sinusoid problem in 3D without adhesion, and then (Johnson, 1995) used for a sinusoid with adhesion. Ciavarella (2015) extended XJM to JKR adhesion, and noticed that the result depends on a higher order spectral moment, i.e., the 6^{th} order spectral moment, which seems to imply more and more "adhesion" when higher frequency components are introduced – a result which is quite counterintuitive, at least if one compares it with our knowledge of pull-off decay, or with Pastewka–Robbins criterion (Pastewka and Robbins (2014)) which instead shows adhesion reduction with increasing slopes at high magnification. One problem may be the assumption of the JKR model, and therefore we shall extend here the Ciavarella (2015) model to the Maugis–Dugdale cohesive adhesion, looking to establish *a rigorous multiscale "Tabor" parameter* in these conditions.

2. The model

The main idea is described in Xu et al. (2014) in detail. Starting from the full contact pressure as if the bodies were stuck to each other, we obtain tensile stresses which are not sustainable in some gaps. These stresses, as coming from a random process, can be approximated near the "summits" of the full contact pressure "surface", in the parabolic forms. Note that some other shapes can also be applied to describe the geometry of the asperity (Ciavarella et al., 2008). This is similar to what is done in asperity theories in approximating asperity summits geometries (Greenwood and Williamson, 1966), but the order of the approximation is completely different. When the real area of contact is nearly the same as the nominal contact area, the XJM model leads to results which are expected to be more accurate than Persson's solution (Xu and Jackson, 2017). Therefore, the accuracy of XJM asperity model is not immediately comparable with the accuracy of the GW model, and our proposed model for adhesion is rather "specular" to the Fuller and Tabor asperity model in the limit near full contact rather than very light contact.

It is commonly accepted that the isotropic rough surfaces can have the following power spectral density (PDF)(Persson et al., 2005):

$$C(q) = \begin{cases} Z(q/q_0)^{-2(H+1)} & q \in [q_0, q_1], \\ 0 \quad \text{elsewhere}, \end{cases} \tag{2}$$

where q_0 and q_1 are the lower and upper cut-off circular wavenumber (2π/wavelength), respectively. H is the Hurst dimension. H has the following relation with the fractal dimension, D: $H = 2 - D$ for 2D profile and $H = 3 - D$ for 3D surface. Since the statistics of an isotropic rough surface is invariant of the measurement direction (Nayak, 1971), the corresponding PSD only depends on the modulus, q, of the wavevector (q_x, q_y) (i.e., the PDF is axisymmetric in the frequency domain). Additionally, the vertical dimension scales differently from the in-plane dimensions, the surfaces associated with the above PDF are referred to as the self-affine fractal rough surfaces.[1] The magnification factor is defined as $\zeta = q_1/q_0$. However, this does not mean that the model is restricted to the power law PSD.

Based on the definition of the spectral moments (Nayak, 1971), then spectral moments of a self-affine surface can be written in the closed-forms: Assuming an isotropic roughness, spectral moments are

$$m_n = \int_{q_0}^{q_1}\int_0^{2\pi} [q\cos(\theta)]^n C(q) q dq d\theta = \int_0^{2\pi} [\cos(\theta)]^n d\theta \int_{q_0}^{q_1} C(q) q^{n+1} dq. \tag{3}$$

[1] Sayles and Thomas (1978) calculated the spectral density functions of many natural surface profiles finding an universal slope (and hence fractal dimension 2.5 in modern terms), which would be not too largely in contrast with present general consensus of fractal dimension being often close to 2.2 (Persson, 2014; Persson and Scaraggi, 2014), and presented experimental relations which span nearly eight decades in wavelength. It should be said that Whitehouse (2001), Borodich and Wang (2013a) and Borodich (2013b) make some critical comments on the use of fractals, although in turn Greenwood (2002) clarifies and improves many statements in Whitehouse (2001). Additionally, the concern of the applicability of fractal technique is also raised up by Zhang et al. (2017). However, our analysis is not assuming any arbitrary "fractal" hypothesis, being solely based on the mechanics of closing gaps near full contact, for which we derived some parametric dependence.

Writing $T(n)=\int_0^{2\pi}[\cos(\theta)]^n d\theta$, we get from the general definition (3), that the spectral moments of order n in the case of the PSD in Eq. (2) are ($n=0,2,4,6$)

$$m_n = ZT(n)q_0^{n+2}\left(\frac{\zeta^{n-2H}-1}{n-2H}\right), \tag{4}$$

where $T(0)=2\pi, T(2)=\pi, T(4)=3/4\pi$ and $T(6)=5/8\pi$.

Then considering the transfer function between the spectrum of the roughness and the corresponding full contact pressure, the first three spectral moments of the full contact pressure "surface" m_{2n}^p are (Ciavarella, 2015; Xu and Jackson, 2017)

$$m_0^p=\frac{1}{2}E^{*2}m_2, \qquad m_2^p=\frac{1}{3}E^{*2}m_4, \qquad m_4^p=\frac{3}{10}E^{*2}m_6, \tag{5}$$

where the superscript "p" stands for quantities relative to the full contact pressure "surface". Note that the units of m_0^p, m_2^p and m_4^p are $\mathbf{Pa^2}$, $[\mathbf{Pa^2/m^2}]$ and $[\mathbf{Pa^2/m^4}]$, respectively. Thus, the dimensionless bandwidth parameter of the full contact pressure "surface" becomes $\alpha^p=\frac{27}{20}m_2m_6/(m_4)^2$ and is generally much lower than the bandwidth parameter, α, for the rough surface itself.[2]

For the full contact pressure "surface", from McCool (1987), we derive the density of asperities η^p, the average radius R^p, the rms amplitude of summits heights σ_s^p and the height of mean summit heights m^p (assuming the mean surface height is zero) as (Xu et al., 2014)

$$\eta^p=\frac{1}{6\sqrt{3}\pi}\frac{m_4^p}{m_2^p}, \qquad R^p=0.375\sqrt{\frac{\pi}{m_4^p}},$$
$$\sigma_s^p=\sqrt{1-\frac{0.9}{\alpha^p}}\sqrt{m_0^p}, \qquad m^p=4\sqrt{\frac{m_0^p}{\pi\alpha^p}}, \tag{6}$$

The above process leads to the modified GW model (Ciavarella, 2016; Xu and Jackson, 2017) which is close to the Persson (2001) solution, where the other advanced asperity models (e.g., the modified Nayak-Bush model and the modified Greenwood model developed in Xu et al. (2014) did not seem to make much difference. Therefore, a much simpler model using the concept of "bearing area" was developed by Ciavarella (2016). In the rough surface contact, the bearing area is referred to the portion of the rough surface (profile) whose height is above a certain level. This concept can also be applied to the full contact pressure "surface". At a given average contact pressure, the full contact pressure "surface" is a mixture of tensile and compressive traction. The tensile portion is referred to as the "bearing area". At nearly complete contact where the average contact pressure is significantly large, the non-contact area should be at large pressures equal to 3/2 the "bearing area" of the full contact pressure "surface" (Manners and Greenwood, 2006). Ciavarella (2016) showed that, if we multiply this by a factor of 4/3, we get exactly the result of Persson (2001) immediately without any integration, and any dependence on the bandwidth parameters. In terms of the dimensionless average pressure ($\overline{p}''=\overline{p}/\sqrt{m_0^p}$), the ratio of the non-contact area, A_{nc}, to the nominal contact area, A_0, is

$$\frac{A_{nc}\left(\overline{p}''\right)}{A_0}=Erfc\left(\frac{\overline{p}''}{\sqrt{2}}\right), \tag{7}$$

where $Erfc()$ is the complementary error function. Eq. (7) is approximately valid in the entire range of pressure (from the initial touch to the complete contact). Xu and Jackson (2017) used more refined models which may be more accurate near full contact, but in the case of adhesion, since the complexity of the problem is much higher, the advantage of approximate results, especially to discuss qualitative dependence on parameters, as we want to do here, is evident.

2.1. The JKR case

We have shown in Ciavarella (2015) that, under a small approximation, the solution is simply of a Persson-like form for loading only, but now to the mean pressure we add a contribution which we identified as $p_0=1.20\left(\frac{K_{Ic}^4}{R_p}\right)^{1/5}$ where K_{Ic} is toughness of the contact. In dimensionless terms,

$$\left(\frac{A_{nc}\left(\overline{p}''\right)}{A_0}\right)_{JKR}^{loading}\simeq Erfc\left(\frac{\overline{p}''+p_0''}{\sqrt{2}}\right). \tag{8}$$

[2] The error in classical asperity theories can be considerable and depend on the Nayak bandwidth (at least for the area load, see Carbone and Bottiglione, 2008), whereas in the "full contact pressure" asperity theory here discussed the results, in the adhesionless case, will be extremely close to Persson (2001), and almost independent on the "full contact pressure" bandwidth parameter α^p, as we shall explain.

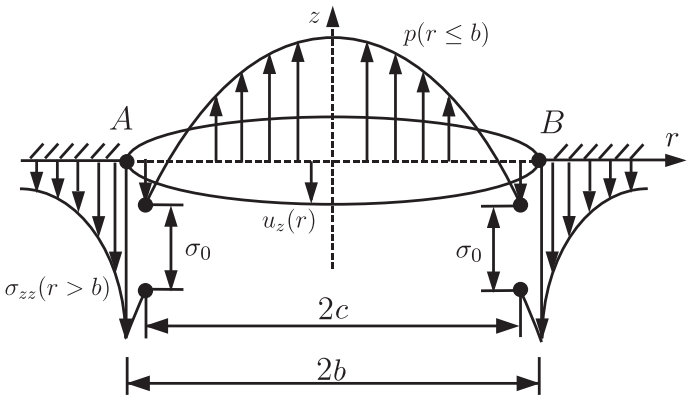

Fig. 1. Geometry of the cohesive crack.

where the dimensionless parameter

$$p_0'' = \frac{p_0}{\sqrt{m_0^p}} = 2.154 \frac{m_6^{1/10}}{m_2^{1/2}} l_a^{2/5}. \tag{9}$$

This p_0'' is the critical dimensionless parameter of the JKR solution in Eq. (8), and is a parameter of "stickiness" in the sense that when p_0'' increases, the area of non-contact decreases rapidly. For a large magnification factor ζ, it is easy to show from the spectral moments of a self-affine fractal surface (Eq. (4)) that (Ciavarella, 2015)

$$p_0'' \sim \zeta^{\frac{2}{5}(2H-1)}, \tag{10}$$

and therefore it increases with magnification ζ if the fractal dimension of the surface is low, as it is the most common case.

Clearly, since the "near full contact" approximation requires strictly speaking that $\bar{p}'' + p_0'' > \xi$ (i.e., a value for which the error function is sufficiently small), the JKR solution makes sense if $p_0'' \ll 1$, as we shall see it is possible with some "non sticky" surfaces at realistic resolutions (see Examples paragraph). However, notice that the Ciavarella (2015) solution in the limit of $p_0'' = 0$ tends to the Persson solution which is approximately valid in the entire range of pressures. This is a suggestion that in the intermediate cases, the requirement that $\bar{p}'' > p_0''$ probably could be relaxed. Still, we don't think we can use the solution in the tensile range, and therefore we will not pretend to estimate pull-off from this. Of course, if we were to make an educated guess prediction, we would suggest that pull-off does increase with p_0''.

3. The cohesive crack - Maugis–Dugdale model

Following the statistical model developed by Xu et al. (2014), the adhesive rough surface contact can be decomposed into a complete contact model and various pressurized cohesive crack model. A schematic representation of a penny-shaped cohesive crack is shown in Fig. 1. The upper and lower crack surfaces are subjected to an axisymmetric normal traction as follows:

$$p(r) = \begin{cases} p_1 - \dfrac{r^2}{2R^p} & r \le c, \\ p_1 - \sigma_0 - \dfrac{r^2}{2R^p} & c < r \le b, \end{cases} \tag{11}$$

where R^p is the radius of pressure surface, $p(r)$ and has the unit of $[m^2/Pa]$. a discontinuous point can be found at $r = c$ due to the uniform cohesive stress of intensity σ_0. At the vicinity of the non-contact region, the superposition of the cohesive crack model and the complete contact model results in positive contact pressure at the contact area. Since the tensile traction in from of the crack tip is obviously less than σ_0. Therefore, the absolute tensile stress in the adhesive rough surface contact should always be less than σ_0. This simplified cohesive stress distribution is commonly referred to as the Dugdale model (Dugdale, 1960), even though it is originally used for the small scale yielding at the crack tips. The general solutions of a penny-shaped crack subjected to an axisymmetric internal traction of arbitrary forms are found by Sneddon (1946) and are tabulated in Maugis (2000).

The pressurized cohesive crack in Fig. 1 can be decomposed into a cohesive crack in the JKR limit and a penny-shaped crack subjected to the Dugdale model within the cohesion zone. According to the analytical solutions tabulated in Appendix A, the normal stress, $\sigma_{zz}(r)$, the upper/lower crack opening displacement (COD), $u_z(r)$, and the stress intensity

factor (SIF), K_I, can be obtained through the superposition:

$$K_I = \frac{2}{\sqrt{\pi b}}\left[p_1 b - \frac{b^3}{3R^p} - \sigma_0\sqrt{b^2-c^2}\right], \tag{12}$$

$$\sigma_{zz}(r \geq b) = \frac{b}{\pi}\frac{K_I}{\sqrt{r^2-b^2}} - \frac{2}{\pi}\left(p_1 - \frac{r^2}{2R^p}\right)\tan^{-1}\left(\frac{b}{\sqrt{r^2-b^2}}\right) - \frac{\sigma_0}{\pi}\tan^{-1}\left(\frac{r^2-2b^2+c^2}{2\sqrt{b^2-c^2}\sqrt{r^2-b^2}}\right) - \frac{2b}{\pi}\sqrt{r^2-b^2} + \frac{\sigma_0}{2}, \tag{13}$$

$$u_z(r \leq b) = \frac{4}{\pi E^*}\left\{\sqrt{b^2-r^2}\left[p_1 - \frac{1}{9R^p}(2r^2+b^2)\right] - \sigma_0\int_{\max(r,c)}^{b}\frac{\sqrt{t^2-c^2}}{\sqrt{t^2-r^2}}dt\right\}. \tag{14}$$

For a crack of radius c, with an annular cohesive zone extending from $r = c$ to $r = b$, see Fig. 1, we need to write two conditions: (1) there is no singularity of normal stresses at the crack tips (A and B in Fig. 1), i.e., $K_I = 0$, and (2) the upper/lower COD, $u_z(r)$, at the end of the cohesive zone is equal to a limit value, $u_z(c) = \delta_t = w/\sigma_0$. The latter condition can either be derived by the J-integral (Maugis, 1992) or based on the definition of the surface energy (Greenwood and Johnson, 1998).

Substituting Eqs. (12) and (14) into the above two conditions, two dimensional governing equations are

$$p_1 b - \frac{1}{3R^p}b^3 - \sigma_0\sqrt{b^2-c^2} = 0, \tag{15}$$

$$\frac{4}{\pi E^*}\sigma_0\left\{\sqrt{b^2-c^2}\left[p_1 - \frac{1}{9R^p}(2c^2+b^2)\right] - \sigma_0(b-c)\right\} - w = 0. \tag{16}$$

Note that the singular term (first term in the right hand side of Eq. (12)) in $\sigma_{zz}(r \geq b)$ is vanishing if Eq. (15) is satisfied.

If we define the dimensionless notations

$$p^* = p_1 / \left(\frac{\pi^2 E^{*2} w^2}{72R^p}\right)^{1/5}, \tag{17}$$

$$b^* = b / \left(\frac{81\pi E^* w (R^p)^2}{16}\right)^{1/5}, \tag{18}$$

$$m = c/b, \tag{19}$$

and a dimensionless parameter (which we later recognize as our "multiscale Tabor parameter near full contact")

$$\sigma_0^* = \sigma_0 / \left[\frac{\pi^2 (E^*)^2 w^2}{72R^p}\right]^{1/5}, \tag{20}$$

we can transform the above system of equations (Eqs. (15) and (16)) into

$$\frac{3}{2}(b^*)^2 + \sigma_0^*\sqrt{1-m^2} - p^* = 0, \tag{21}$$

$$\frac{1}{2}\sqrt{1-m^2}(2m^2+1)(b^*)^3 - \left[p^*\sqrt{1-m^2} - (1-m)\sigma_0^*\right]b^* + \frac{1}{\sigma_0^*} = 0. \tag{22}$$

The above system of equation can be partially proved by its asymptotic solutions when $\sigma_0^* \to 0$ and ∞. As the dimensionless parameter, $\sigma_0^* \to 0$, the surface energy on the crack surfaces vanishes. Therefore, Eq. (22) related to the energy equilibrium does not exist and Eq. (21) approaches the non-adhesive limit, see Eqs. (B.3) and (B.4) in Appendix B. In another extreme where $\sigma_0^* \to \infty$, Eq. (C.4) in Appendix C is the asymptote of Eqs. (21) and (22).[3]

Similar to the JKR limit in Appendix B, the Maugis–Dugdale model is also nonlinear. For a given p^*, b^* and m depend on σ_0^* only. The above set of dimensionless equations has maximum two real roots, only one of which corresponds to a stable solution. This conclusion will be confirmed by the numerical results illustrated below. The stability of the cohesive crack is explored now.

[3] Replacing σ_0^* in Eq. (22) by Eq. (21).

For a fixed load condition (i.e., p^* is constant), the stability of the cohesive crack in the static equilibrium can be determined based on the Griffith's crack theory (Maugis, 2000). The strain energy release rate is $G = u_z(c)\sigma_0$ (Maugis, 1992). Defining the dimensionless strain energy release rate, $G^* = G/w$, the expression of G^*can be obtained from Eq. (22):

$$G^* = \sigma_0^*\left[p^*\sqrt{1-m^2} - (1-m)\sigma_0^*\right]b^* - \frac{1}{2}\sigma_0^*\sqrt{1-m^2}(2m^2+1)(b^*)^3, \tag{23}$$

and

$$\left(\frac{\partial G^*}{\partial b^*}\right)\Big|_{p^*} = \sigma_0^*\left[p^*\sqrt{1-m^2} - \sigma_0^*(1-m)\right] + \sigma_0^* b^*\left[\sigma_0^* - p^*\frac{m}{\sqrt{1-m^2}}\right]\frac{\partial m}{\partial b^*} - \frac{3}{2}\sigma_0^*\sqrt{1-m^2}(2m^2+1)(b^*)^2 + \frac{1}{2}\sigma_0^*\frac{m}{\sqrt{1-m^2}}\frac{\partial m}{\partial b^*}(2m^2+1)(b^*)^3 - 2\sigma_0^* m\sqrt{1-m^2}(b^*)^3\frac{\partial m}{\partial b^*}, \tag{24}$$

where the partial derivative $\frac{\partial m}{\partial b^*}$ is directly obtained from Eq. (21)

$$\frac{\partial m}{\partial b^*} = \frac{3b^*}{m(\sigma_0^*)^2}\left[p^* - \frac{3}{2}(b^*)^2\right]. \tag{25}$$

The cohesive crack is stable when $\partial G^*/\partial b^* \le 0$ and when $\partial G^*/\partial b^* > 0$ the crack is unstable.

3.1. Full cohesion limit: $c = 0$

The Maugis–Dugdale transition discussed above implicitly assumes that the cohesion zone is restricted within the annulus: $0 < c \le r \le b$ (Jin et al., 2016a; 2016b). As $c \to 0$ ($m \to 0^+$), the cohesion zone is extended to the entire crack surface. In this case, the dimensionless crack size, b^*, can be directly solved from Eq. (21):

$$b^* = \sqrt{\frac{2}{3}\left(p^* - \sigma_0^*\right)}. \tag{26}$$

This solution holds until the COD inequality condition is satisfied, which is also equivalent to write that the strain energy release rate $G^* < 1$. Substituting $m = 0$ and Eq. (21) into Eq. (23), the complete form of the inequality reads as

$$G^* = \sigma_0^*\left[\frac{2}{3}(p^* - \sigma_0^*)\right]^{3/2} < 1. \tag{27}$$

3.2. Hysteresis loop of pressurized cohesive crack

Figs. 2 and 3 illustrate the evolution of b^* and m of the Maugis–Dugdale model and the full cohesion limit associated with different σ_0^*. The loading stage of the cohesive crack is related to the loading stage of the rough surface contact where the dimensionless radius of each cohesive crack, b^*, and the dimensionless pressure, p^*, are monotonically decreased. Similarly, b^* and p^* are increased monotonically in the unloading stage of the cohesive crack. Only one loading-unloading cycle are illustrated in Figs. 2 and 3. For the sake of the presentation, Figs. 2(a) and 3(a) associated with $\sigma_0^* = 5$ are used as the representative results of the evolution of b^* and m since all the important branches are visible. The rest of the figures due to the change of σ_0^* will be explained later.

The entire loading stage can be divided into four branches, namely, A-G, G-B, B-C and C-D. In the A-G branch, non-negative roots of Maugis–Dugdale model (b^* and m) are unique and are decreased monotonically with the decreasing of p^*. The A-G branch is stable based on Eq. (24) (see also the legend in Figs. 2(a) and 3(a)). When $p^* < p_G^*$, the Maugis–Dugdale model has dual (non-negative) roots and the loading stage follows branch G-B since (1) it is a stable branch and (2) b^*, as well as m, is continuous at point G. At point B, a negative perturbation from $p^* = p_B^* = p_C^*$ results in the snap-in, i.e., an instantaneous closure of the cohesive crack within B-C branch where p^* is kept constant. Within C-D branch, the cohesive crack remains in closure, see Fig. 2(a) and the cohesive zone is instantaneously extended to the entire crack surfaces, see Fig. 3(a).

The entire unloading stage can be divided into four branches, namely, D-E, E-F, F-G and G-A. The cohesive crack remains in closure within the D-E branch until point E is reached where the cohesive crack is nucleated. The corresponding p^* at E can be solved analytically from the full cohesion limit:

$$p_E^* = \sigma_0^*. \tag{28}$$

The entire E-F branch in the full cohesion limit where the uniform cohesive stress is extended to the entire crack surfaces. Along the E-F branch the cohesive crack is propagating ($G^* < 1$) with $m = 0$ until point F is reached. F is the intersection of

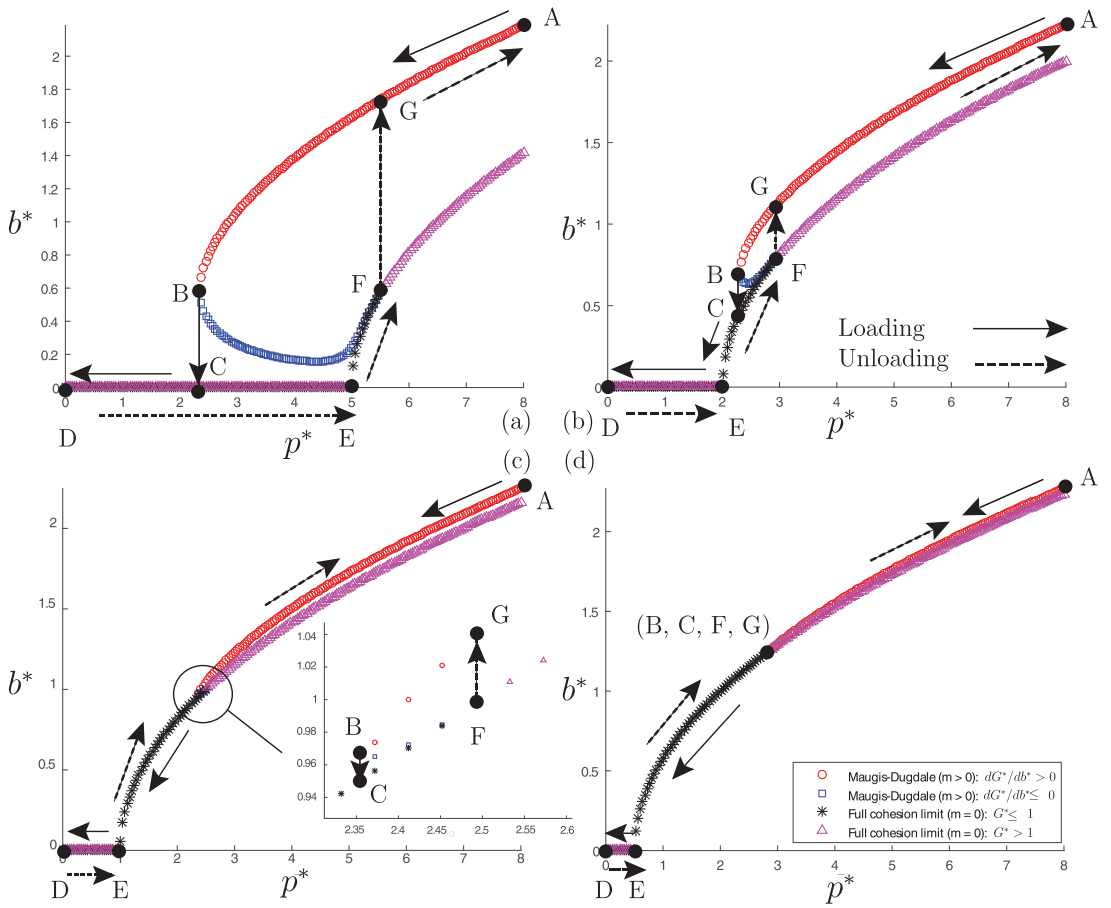

Fig. 2. Evolution of b^* of a cohesive crack during one loading-unloading cycle with (a) $\sigma_0^* = 5$, (b) $\sigma_0^* = 2$, (c) $\sigma_0^* = 1$ and (d) $\sigma_0^* = 0.5$.

the full cohesion limit and the unstable branch of the Maugis–Dugdale transition. Therefore, the root, $p^* = p_F^* = p_G^*$, results in $G^* = 1$ in the full cohesion limit and p_F^* is available in the closed-form:

$$p_F^* = \sigma_0^* + \frac{3}{2}(\sigma_0^*)^{-2/3}. \tag{29}$$

Because point F is unstable, the pull-off occurs, i.e., the cohesive crack is propagating instantaneously where p^* is kept constant within the branch $F-G$. This unstable propagation stops at the next stable stage at point G of the Maugis–Dugdale model. After point G ($p^* > p_G^*$), the unloading and loading stages are reversible. Consequently, the hysteresis/energy dissipation of the cohesive crack associated with $\sigma_0^* = 5$ occurs within $p^* \in [p_B^*, p_G^*]$.

When $\sigma_0^* = 2$, the unstable points B and F are approaching to each other, see Fig. 2(b). At the unstable point B, an instantaneous jump onto the full cohesive (E-F) branch (instead of a snap-in) occurs. Following C-E branch, the crack is completely closed when $p^* < p_E^*$. The unloading stage follows the same branches in Figs. 2(a) and 3(a). It is obvious that the energy dissipation only occurs within a smaller range, see Fig. 2(b). The decrease of the hysteresis range is confirmed in the rest of the figures in Fig. 2 where σ_0^* is even smaller. This trend shows that σ_0^* is correlated with the hysteresis/energy dissipation of the single cohesive crack.

When $\sigma_0^* = 1$, the instantaneous jump at points B and F can still be visualized in the detailed plot in Fig. 2(c). However, as σ_0^* is decreased to 0.5, the points B, C, F and G are visually "coincident", see Fig. 2(d). According to the numerical results, the instantaneous jump always occurs at point B whenever $\sigma_0^* > 0$ and the drop of the crack size due to the jump from B to C is reduced with the decrease of σ_0^*. It is expected that as $\sigma_0^* \to 0$, points B, C, F and G merge into one and the loading-unloading cycle becomes fully reversible (i.e., no hysteresis occurs).

Important observations of the hysteresis loading-unloading loop of the cohesive crack are summarized blow:

Loading stage:

1. the snap-in (instantaneous closure) of the cohesive crack occurs when $p^* = \min(p_B^*, \sigma_0^*)$;
2. the instantaneous jump onto the full cohesion limit occurs if $p^* = p_C^*$ and $p_B^* > p_E^*$.

Unloading stage:

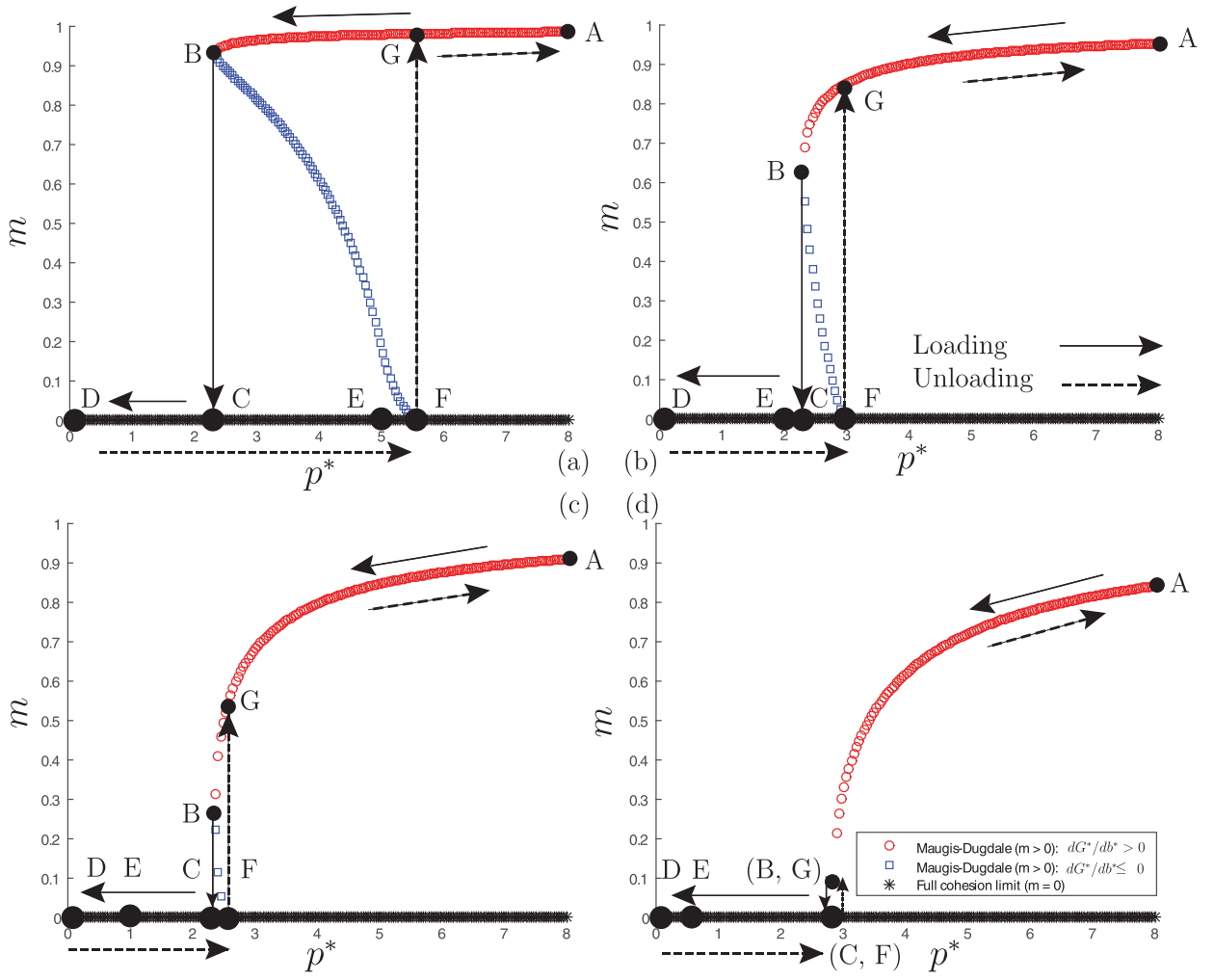

Fig. 3. Evolution of m of a cohesive crack during one loading-unloading cycle with (a) $\sigma_0^* = 5$, (b) $\sigma_0^* = 2$, (c) $\sigma_0^* = 1$ and (d) $\sigma_0^* = 0.5$.

1. the cohesive crack has hysteretic loading-unloading cycle as long as the unloading stage starts at $p^* < p_B^*$;
2. the unloading and loading stages are reversible within $[p_F^*, \infty]$ after the instantaneous jump at $p^* = p_F^*$ from the full cohesion limit to the Maugis–Dugdale transition.

It should be noticed that the unloading stage, illustrated in Figs. 2 and 3, starts from $p^* = 0$. If the cohesive crack is unloaded at a positive minimum, $p_D^* > 0$, we may have the following three possibilities:

- $p_D^* < p_E^*$: cohesive crack is unloaded from closure and the unloading stage follows same path in Fig. 2 (i.e., D-E-F-G-A);
- $p_E^* < p_D^* < p_B^*$: cohesive crack is unloaded from positive size in the cohesion limit follows by the unloading path: D-F-G-A;
- $p_D^* \geq p_B^*$: cohesive crack is unloaded with a finite crack size followed by a reversible unloading stage, i.e., loading-unloading cycle is no longer hysteresis.

After the removal of the redundant roots in Fig. 2, the dimensionless crack radius b^* vs. p^* curves associated with different σ_0^*, as well as the non-adhesive limit and the JKR limit, are illustrated in Fig. 4(a) (loading stage) and Fig. 4(b) (unloading stage). Note that the unloading stage starts after p^* is vanishing. It is clear that Maugis–Dugdale transition has the tendency to approach the non-adhesive (DMT) limit and the JKR limit as $\sigma_0^* \to 0$ and $\sigma_0^* \to \infty$.

3.3. The cohesive crack area

With the solution of b^* and m, the corresponding dimensionless crack area, where $\sigma_0^* > 0$, can be determined easily by

$$A_i^* = \pi (b^*)^2. \tag{30}$$

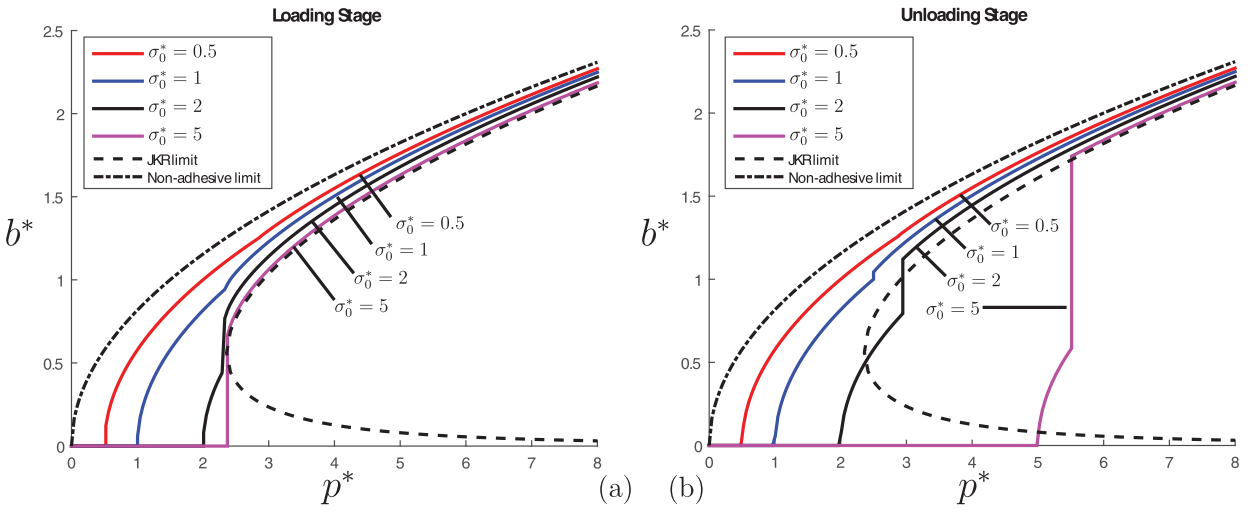

Fig. 4. Dimensionless crack radius b^* vs. p^* associated with different σ_0^* at (a) loading and (b) unloading stage. p^* is vanishing at the end of loading stage.

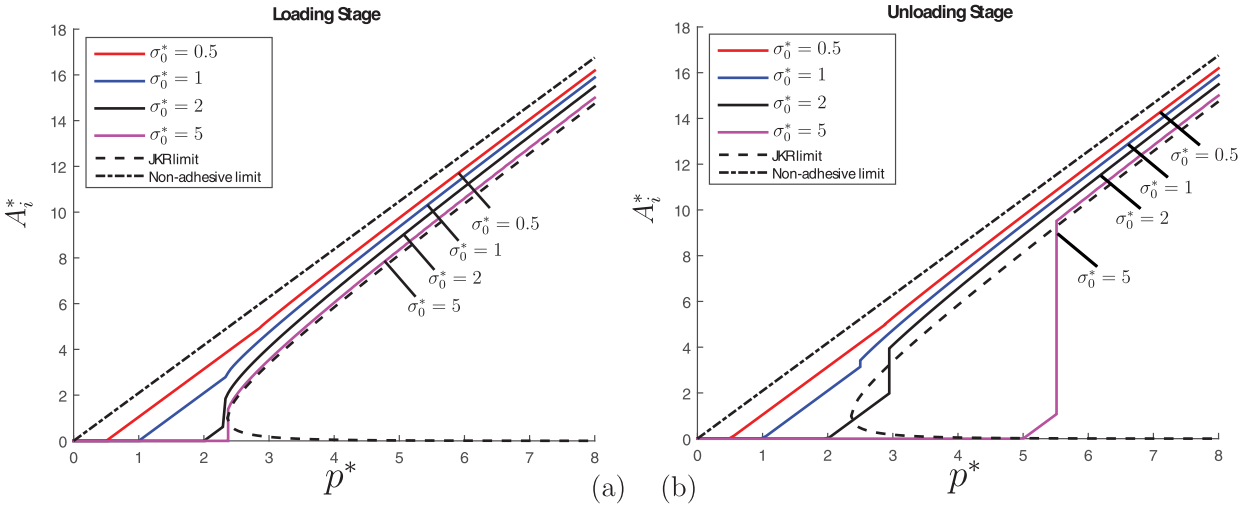

Fig. 5. Dimensionless crack area A^* vs. p^* associated with different σ_0^* at (a) loading and (b) unloading stage. p^* is vanishing at the end of loading stage.

where A_i is normalized by $\left[\frac{81\pi E^* w (R^p)^2}{16}\right]^{2/5}$.

When $\sigma_0^* \to 0$, the crack radius degenerates to the non-adhesive limit (see Eq. (B.4) in Appendix A). As $\sigma_0^* \to \infty$, then the crack area in the JKR limit is found (see Appendix B). The corresponding A_i^* vs. p^* curves, as well as the asymptotic solutions when $\sigma_0^* \to 0$ and $\sigma_0^* \to \infty$, are plotted in Fig. 5. As σ_0^* is increased, A_i^* vs. p^* transits from the non-adhesive limit to the JKR limit.

3.4. A multiscale Tabor parameter for nearly full contact

According to Fig. 5, we have recognized that the parameter

$$\sigma_0^* = \frac{\sigma_0}{\left(\frac{\pi^2 E^{*2} w^2}{72 R^p}\right)^{1/5}} = \frac{\sigma_0}{E^*} \frac{1}{0.647 l_a^{2/5} m_6^{1/10}}, \tag{31}$$

is what Tabor parameter gives for the adhesive Hertzian contact where the status transits from a hysteretic behaviour "JKR regime" at high σ_0^*, to a non-hysteretic or "DMT regime" at low σ_0^*. We may therefore call this the "Tabor multiscale" parameter (near full contact).

Notice that the original standard Tabor parameter can be related to the ratio of the contact area to process zone with stress close to theoretical strength. Hence, a large value corresponds to the Griffith theory when condition of "small scale

yielding" apply in standard Linear Elastic Fracture Mechanics. The original version of the Tabor parameter is easily applied to multi-asperity contact models where the characteristic contact area is taken either as its mean value (which is likely to be load-independent also), or a mean radius, like is done by Persson and Scaraggi (2014). Instead, here we find a new Tabor parameter as the ratio of process zone to characteristic separation radius bmin (see App. C).

For the nearly complete rough surface contact, each non-contact region is "nucleated" due to the surface traction where $p_1 = p - \bar{p}$. The asperity height of the pressure "surface" is p. When $\sigma_0^* < 1$, the full cohesion limit can be used to approximate the Maugis–Dugdale model where $p^* < p_B^*$, see Figs. 4 and 5. We find that the contact becomes nearly non-hysteretic, and a good approximation for the area of each non-contact region (cohesive crack) is Eq. (26). The dimensional form of Eq. (26) is

$$\pi b^2 = 3\pi R^p[(p-\overline{p}) - \sigma_0] \quad \text{for } (p-\overline{p}) < p_B. \tag{32}$$

Defining $\sigma_0'' = \sigma_0/\sqrt{m_0^p}$, then the low Tabor solution (DMT, $\sigma_0^* \lesssim 1$) is close to a Persson shifted solution with

$$\left(\frac{A_{nc}\left(\overline{p}''\right)}{A_0}\right)_{DMT} \simeq Erfc\left(\frac{\overline{p}'' + \sigma_0''}{\sqrt{2}}\right), \tag{33}$$

whereas at high Tabor parameter, the JKR solution (during loading only) in Eq. (8) should be used.

Therefore the solution at low Tabor is equivalent to that at high Tabor, when σ_0'' replaces p_0''. Obviously, when $\sigma_0'' \to 0$ we return to the adhesionless solution.

Notice that

$$\sigma_0'' = \sqrt{2}\frac{\sigma_0}{E^* m_2^{1/2}} = 0.425\sigma_0^* p_0''. \tag{34}$$

Therefore, close to $\sigma_0^* = 1$ we have a transition and then σ_0'' continues to decrease with σ_0^*.

The problem with the JKR solution (Ciavarella, 2015) was that apparently $p_0'' \sim \zeta^{\frac{2}{5}(2H-1)}$ increases without limit if we consider a spectrum of roughness and increase "magnification" (i.e. take a larger upper cut-off wavenumber $q_1 = \zeta q_0$): on the one hand, this seems to suggest that contact becomes more "sticky", but on the other hand, the solution we give is an approximation at higher and higher pressure, so it is simply suggesting a trivial result: full contact. This is clearly paradoxical, since it would mean that any surface, if looked at sufficiently large magnification, would be "sticky".

However, we have seen that the full cohesive solution depends also on the "Tabor multiscale" parameter which scales as $\sigma_0^* \sim \zeta^{-\frac{3-H}{5}}$ for a large ζ, see Eq. (4), and therefore decreases with magnification. For low $\sigma_0^* < 1$ the correct stickiness parameter becomes σ_0'' which therefore decreases with magnification, and it no longer depends on the 6th order spectral moment — only on the rms slope of the surface. As a first approximation, neglecting the crossover regime where the "stickiness" will depend on both parameters, we are suggesting that the correct stickiness parameter which holds at all magnification is

$$s'' = \min\left(p_0'', \sigma_0''\right), \tag{35}$$

Note that the above stickiness parameter is valid for both the lower and higher magnification ranges. Its validity within the intermediate magnification range needs further investigation in our future study using a complete adhesive statistical model.

The higher the stickiness parameter s'' is, the more sticky the rough surface is. Notice that if we simplify the criterion with this "min" function, the transition does not occur "exactly" at $\sigma_0^* = 1$ but at $\sigma_0^* = \frac{1}{0.425} = 2.35$ and this occurs for magnification ζ_{trans}, this shows the highest stickiness parameter can be

$$\left(s''\right)_{\max} = 0.425 p_0''(\zeta_{trans}).$$

All this can be clarified by Fig. 6. In blue dashed line, we have the "Tabor parameter" σ_0^* which decreases with magnification, and for this case of qualitative discussion, becomes 2.35 at $\zeta_{trans} \simeq 10^{2.5}$. We have then, with dashed lines, the p_0', σ_0' power laws (one increases, the other decreases with magnification), and the stickiness parameter $s'' = \min\left(p_0'', \sigma_0''\right)$ is indicated with bold black curve. Naturally this plot is entirely qualitative, and the values are indicative — we shall see examples in the next paragraph. We have used in the plot $H = 0.8$ which is a common case, so the slope of the power law is actually quantitatively correct.

Since the "stickiness parameter" we suggest first grows and then decreases with magnification, the behaviour in the end is more physical – it seems to suggest that adhesion is at least less sensitive to the truncation of the spectrum as it first appeared with the JKR solution. Strictly speaking, the results associated with the infinite wavenumber should always be a complete destruction of adhesion, but this end should be further investigated.

In absolute terms, suppose $\sigma_0 = 0.05E^*$ as it is common for elastic solids, then

$$\sigma_0'' = \sqrt{2}\frac{0.05}{\sqrt{m_2}},$$

and this is not very large at very large magnification where for example $m_2 = 1$, $\sigma_0'' = 0.05$ and the area of contact will be similar to that without adhesion.

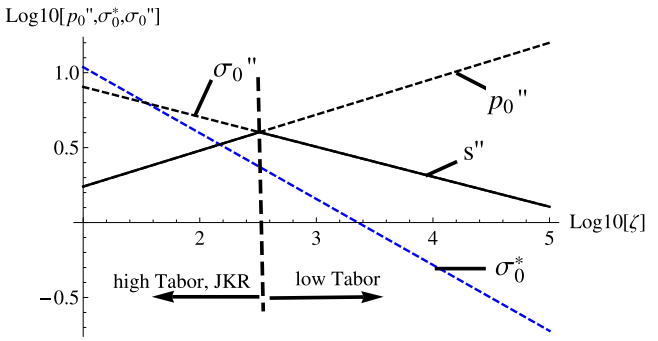

Fig. 6. The stickiness parameter.

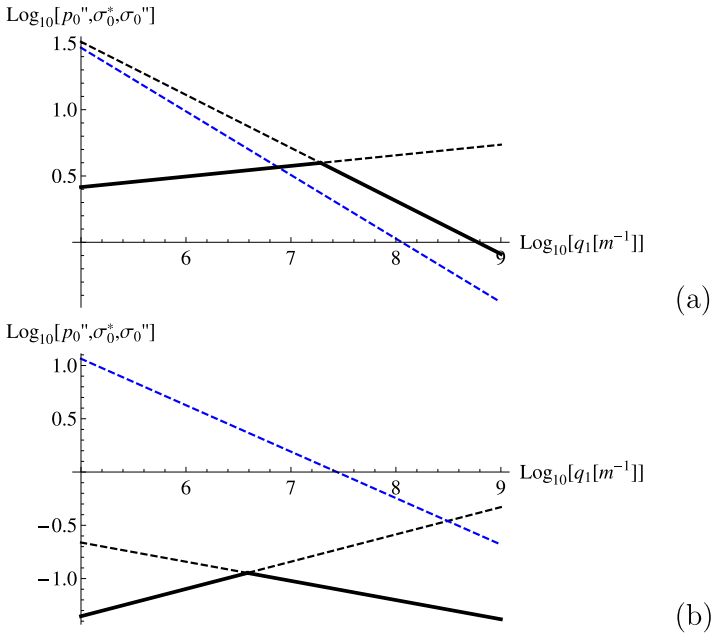

Fig. 7. The prediction of the stickiness parameter for surfaces of Plexiglas in Fig. 17 of Persson et al. (2005) (a) and sandblasted steel of Carbone and Putignano (2014) (b) using the assumption that Lennard–Jones potential applies, $l_a/a_0 = 0.05$ with atomic distance $a_0 = 10^{-9}m$ and $\frac{\sigma_0}{E^*} \simeq 0.05$. Dashed lines are the p_0'' (ascending trend) and σ_0'' (descending trend) power laws. The stickiness parameter $s'' = \min\left(p_0'', \sigma_0''\right)$ is indicated with bold black curve. Blue dashed line is Tabor parameter.

4. Real surfaces

We consider two examples of typical self-affine surfaces, for which the power spectrum is a power law shown in Eq. (2). Let us first consider the surface in Fig. 17 of Persson et al. (2005). It is a Plexiglas surface measured (using an AFM) at two different resolutions over two different surface areas $20 \times 20\mu m$ and $100 \times 100\mu m$ wide. From the data, we have $H = 0.6$, and $Z = 10^{-25.8} \times \left(10^5\right)^{2(0.6+1)} \simeq 1.5849 \times 10^{-10}\left[m^4\right]$. Since the spectral moments m_2, m_4, m_6 depend only on the high wavenumber tail $q_1 = \zeta q_0$, we have

$$m_2 \sim q_1^{2-2H}, \qquad \frac{m_6}{m_2} \sim q_1^4. \tag{36}$$

Let us also consider the data of Carbone and Putignano (2014) who also have two measurements at different resolutions a surface of steel, roughened by sandblasting. PSD is measured at low resolutions by confocal microscope and at high resolutions by AFM. The Hurst exponent is estimated as $H = 0.82$: $Z \simeq 10^{-21.8} \times \left(10^5\right)^{2(0.82+1)}[m^4] = 2.51 \times 10^{-4}[m^4]$.

Hence, suppose adhesion to correspond to an elastic solid for which we use a Lennard–Jones potential, $l_a/a_0 = 0.05$ with atomic distance $a_0 = 10^{-9}$ m and suppose also $\frac{\sigma_0}{E^*} \simeq 0.05$, the comparison of the "stickiness" of the two surfaces is shown in Fig. 7 (a,b).

Clearly, the Plexiglas surface is a lot stickier at all magnifications and at both "low Tabor" and "high Tabor" regimes. However, the low Tabor regime becomes significant at wavenumbers just beyond 10^7, and stickiness seems to persists also at atomic scale. With the steel surface, stickiness is much lower, although the transition occurs a little earlier.

5. Conclusion

We have derived a Tabor parameter for the solution of rough contact near full contact. It involves the radius of full contact pressure "asperities", and not the radius of the real asperities. It is shown, also by some examples, that the Tabor parameter decreases continuously when increasing resolution of measuring instruments and include finer scales in the analysis. We have proposed a stickiness parameter which first increases with resolution, and then decreases when the new Tabor parameter is decreased to less than about 2. The JKR solution is more appropriate at low resolutions and, for one example of a Plexiglas surface, leads to a large deviation from the adhesionless solution, which are not significantly reduced when the low Tabor solution is used. For a metal sandblasted surface, the JKR solution leads to a much smaller deviation from the adhesionless solution, and the low Tabor correction is not needed even at the highest resolution of the AFM measurements.

Appendix A. Sneddon's solutions for the pressurized penny-shaped crack

Consider a penny-shaped crack embedded inside an infinite body. The cylindrical coordinates, $r\theta z$, are chosen with the original located at the center of the crack. The notations adopted in Maugis (2000) are used in the rest of the appendix. The crack surfaces are parallel to the $z=0$ plane. The boundaries at the infinity are stress free. The radius of the crack is a and the crack surfaces are subjected to the axisymmetric normal traction, $p(r)$. The state of stress and the displacement components are solved analytically by Sneddon (1946). The normal stress, $\sigma_{zz}(r\geq a)$, in front of the crack tip and the crack surface normal displacements, $u_z(r\leq a)$, have the following forms:

$$\sigma_{zz}(r)=\frac{2}{\pi}\left[\frac{g(a)}{\sqrt{r^2-a^2}}-\int_0^a\frac{g'(t)dt}{\sqrt{r^2-t^2}}\right], \tag{A.1}$$

$$u_z(r)=\frac{4}{\pi E^*}\int_r^a\frac{g(t)dt}{\sqrt{t^2-r^2}}. \tag{A.2}$$

where

$$g(t)=\int_0^t\frac{sp(s)}{\sqrt{t^2-s^2}}, \tag{A.3}$$

$$g'(t)=p(0)+t\int_0^t\frac{p'(s)ds}{\sqrt{t^2-s^2}}. \tag{A.4}$$

The corresponding stress intensity factor[4] (SIF), K_I, is

$$K_I=\frac{2}{\sqrt{\pi a}}\int_0^a\frac{rp(r)dr}{\sqrt{a^2-r^2}}. \tag{A.5}$$

The above elementary solutions are applied to solve the following pressurized crack problems.

A1. Case I: parabolic normal traction

Consider $p(r)$ of the following form:

$$p(r)=p_0-\frac{\kappa}{2}r^2.$$

Then, $\sigma_{zz}(r)$, $u_z(r)$ and K_I are

$$\sigma_{zz}(r)=\frac{2}{\pi}\left[\frac{\left(p_0a-\frac{1}{3}\kappa a^3\right)}{\sqrt{r^2-a^2}}-\left(p_0-\frac{\kappa}{2}r^2\right)\tan^{-1}\left(\frac{a}{\sqrt{r^2-a^2}}\right)-a\kappa\sqrt{r^2-a^2}\right], \tag{A.6}$$

$$u_z(r)=\frac{4}{\pi E^*}\sqrt{a^2-r^2}\left[p_0-\frac{1}{9}\kappa\left(2r^2+a^2\right)\right], \tag{A.7}$$

$$K_I=2\sqrt{\frac{a}{\pi}}\left(p_0-\frac{\kappa}{3}a^2\right). \tag{A.8}$$

[4] The stress intensity factor is defined as follows: $K_I=\lim_{r\to a^+}\sigma_{zz}(r)\sqrt{2\pi(r-a)}$.

A2. Case II: constant normal traction near the crack tip

Consider $p(r)$ of the following form (Maugis, 2000):

$$p(r) = \begin{cases} p_0 & c < r \le a, \\ 0 & r \le c. \end{cases}$$

The responses of $\sigma_{zz}(r)$, $u_z(r)$ and K_I are[5]:

$$\sigma_{zz}(r) = \frac{2}{\pi}\frac{p_0\sqrt{a^2-c^2}}{\sqrt{r^2-a^2}} - \frac{1}{2}p_0 + \frac{p_0}{\pi}\tan^{-1}\left(\frac{r^2-2a^2+c^2}{2\sqrt{a^2-c^2}\sqrt{r^2-a^2}}\right), \tag{A.9}$$

$$u_z(r) = \frac{4}{\pi E^*}\int_{\max(r,c)}^{a}\frac{p_0\sqrt{t^2-c^2}dt}{\sqrt{t^2-r^2}}, \tag{A.10}$$

$$K_I = \frac{2}{\sqrt{\pi a}}p_0\sqrt{a^2-c^2}. \tag{A.11}$$

A3. Case III: constant normal traction

This case is a special case when $c = 0$ in case II and the response of $\sigma_{zz}(r)$, $u_z(r)$ and K_I can be obtained from the elementary solutions (Maugis, 2000):

$$\sigma_{zz}(r) = \frac{2p_0}{\pi}\left[\frac{a}{\sqrt{r^2-a^2}} - \sin^{-1}\left(\frac{a}{r}\right)\right] \tag{A.12}$$

$$u_z(r) = \frac{4}{\pi E^*}p_0\sqrt{a^2-r^2}, \tag{A.13}$$

$$K_I = 2\sqrt{\frac{a}{\pi}}\sigma_0. \tag{A.14}$$

Appendix B. Non-adhesive limit

In the non-adhesive limit where w is vanishing, the Tabor's parameter, $\sigma_0^* \to 0$. The requirement of the zero singularity at the crack tip results in (Xu et al., 2014)

$$p_0 = \frac{1}{3}\frac{b^2}{R^p}. \tag{B.1}$$

The crack area becomes

$$A_i = 3\pi R^p p_0. \tag{B.2}$$

Substituting the dimensionless notations in Eqs. (17) and (18) into the above three equations, the dimensionless forms of p_0 and A_i are

$$p^* = \frac{3}{2}(b^*)^2, \tag{B.3}$$

$$A_i^* = \frac{2}{3}\pi p^*. \tag{B.4}$$

In the original Maugis–Dugdale model (Maugis, 1992), as the Tabor's parameter is decreased, the asymptotic contact area approach the DMT limit which is lightly different from the Hertzian theory (non-adhesive limit). Similarly, the DMT limit of A_i and V_i may also exist in the cohesive crack model. The derivation of the DMT limit in the Hertzian contact (Derjaguin et al., 1975; Maugis, 1992; Pashley, 1984) relies on the assumption that (i) the cohesion zone is extended to infinity and (ii) the interfacial gap (outside the contact area) and the contact pressure (inside the contact area) are the same as that in the Hertzian theory. Then the total load in the DMT limit is lower than that in Hertzian contact theory by an amount equaling the cohesive force outside the contact area. Since the cohesion zone in the cohesive crack only varies between 0 and b, only the second assumption can be applied to the cohesive crack problem and it results in the same A_i as that in the non-adhesive limit. Therefore, the DMT limit is the same as the non-adhesive limit in the cohesive crack model.

[5] Similar results can be found in pp. 178–179 in Maugis (2000) but with typos in Eq. (3.128).

Appendix C. JKR limit

In the adhesive Hertzian contact, the concept of the JKR limit is referred to as the contact status where the cohesion zone is vanishing (Johnson et al., 1971). In the fracture mechanics, the edges of the adhesive contact in the JKR limit is equivalent to the Griffith crack (Maugis, 2000) where the singularity of the normal stress is allowed. Due to the vanishing of the cohesion zone, the normal traction on the crack surfaces is degraded into $p(r) = p_0 - \frac{\kappa^p}{2} r^2$ where $r \le b$ and the corresponding SIF is (Ciavarella, 2015):

$$K_I = \frac{2\sqrt{b}}{\sqrt{\pi}}\left(p_0 - \frac{1}{3}\kappa^p b^2\right). \tag{C.1}$$

The strain energy release rate of a Griffith crack is (only upper portion is taken into consideration) (Ciavarella, 2015)

$$G = w = \frac{K_I^2}{2E^*}. \tag{C.2}$$

Combining Eqs. (C.1) and (C.2), the crack radius can be solved from the following nonlinear equation (Ciavarella, 2015)

$$p_0 = \frac{1}{3}\kappa^p b^2 + \sqrt{\frac{\pi E^* w}{2b}}. \tag{C.3}$$

Substituting the dimensionless notations in Eqs. (17) and (18), the governing equation [6] in the JKR limit is obtained:

$$p^* = \frac{3}{2}(b^*)^2 + \sqrt{\frac{2}{b^*}}. \tag{C.4}$$

The minimum value of p^* is can be found as

$$p^*_{\min} = \frac{3}{2}\left(\frac{\sqrt{2}}{6}\right)^{4/5} + \sqrt{2}\left(\frac{\sqrt{2}}{6}\right)^{-1/5} \approx 2.3602. \tag{C.5}$$

Ciavarella (2015) also defined $b_{\min} = \left(\frac{3}{8}\sqrt{\pi}\right)^{2/5}(R^p K_{Ic})^{2/5}$, and in the present notation, $b^*_{\min} = \frac{\left(\frac{3}{8}\sqrt{\pi}\right)^{2/5}}{\left(\frac{81\pi}{2\times 16}\right)^{1/5}} = 0.561$.

Based on Eq. (C.2), the dimensionless strain energy release rate, G^*, in the JKR limit is

$$G^* = \frac{1}{8} b^* \left[2p^* - 3(b^*)^2\right]^2. \tag{C.6}$$

For the fixed load condition (p^* is constant) and $p^* > p^*_{\min}$, the stability of the cohesive crack in the JKR limit is $dG^*/db^* \le 0$, i.e.,

$$\frac{3(b^*)^2}{2} \le p^* \le \frac{15(b^*)^2}{2}, \tag{C.7}$$

and the cohesive crack becomes unstable if the above criterion is not satisfied.

The dimensionless crack area determined based on the definition after b^* is solved from Eq. (C.4):

$$A_i^* = \pi (b^*)^2. \tag{C.8}$$

References

Borodich, F.M., 2013b. Fractal nature of surfaces. In: Wang, Q.J., Chung, Y.-W. (Eds.), Encyclopedia of Tribology, vol. 2. Springer, pp. 1264–1269.
Borodich, F.M., Wang, Q.J., 2013a. Fractal geometry. In: Encyclopedia of Tribology, vol. 2. Springer, p. 1258-1264.
Carbone, G., Bottiglione, F., 2008. Asperity contact theories: do they predict linearity between contact area and load? J. Mech. Phys. Solids 56 (8), 2555–2572.
Carbone, G., Putignano, C., 2014. Rough viscoelastic sliding contact: theory and experiments. Phys. Rev. E 89 (3), 032408.
Ciavarella, M., 2015. Adhesive rough contacts near complete contact. Int. J. Mech. Sci. 104, 104–111.
Ciavarella, M., 2016. Rough contacts near full contact with a very simple asperity model. Trib. Int. 93, 464–469.
Ciavarella, M., Greenwood, J.A., Paggi, M., 2008. Inclusion of "interaction in the greenwood and williamson contact theory. Wear 265 (5), 729–734.
Derjaguin, B.V., Muller, V.M., Toporov, Y.P., 1975. Effect of contact deformations on the adhesion of particles. J. Colloid Interface Sci. 53, 314.
Dugdale, D.S., 1960. Yielding of steel sheets containing slits. J. Mech. Phys. Solids 8 (2), 100–104.
Fuller, K.N.G., Tabor, D., 1975. The effect of surface roughness on the adhesion of elastic solids. Proc. R. Soc. Lond. A 345 (1642), 327–342.
Greenwood, J.A., 2002. Comments on fractal or fiction by D.J. Whitehouse [Wear 249 (2001) 345–353]. Wear 252 (9–10), 842–843.
Greenwood, J.A., Johnson, K.L., 1998. An alternative to the Maugis model of adhesion between elastic spheres. J. Phys. D Appl. Phys. 31 (22), 3279.
Greenwood, J.A., Williamson, J.B.P., 1966. Contact of nominally flat surfaces. Proc. R. Soc. Lond. A295, 300–319.
Jin, F., Guo, X., Wan, Q., 2016. Revisiting the Maugis–Dugdale adhesion model of elastic periodic wavy surfaces. J. Appl. Mech. 83 (10), 101007.

[6] Eq. (C.4) can be adapted into

$$\frac{3}{2}t^5 - p^* t + \sqrt{2} = 0 \quad \text{where} \quad t = \sqrt{b^*},$$

and solved by the polynomial solver.

Jin, F., Wan, Q., Guo, X., 2016. A Double–Westergaard model for adhesive contact of a wavy surface. Int. J. Solids Struct. 102, 66–76.
Johnson, K.L., 1995. The adhesion of two elastic bodies with slightly wavy surfaces. Int. J. Solids Struct. 32 (3–4), 423–430.
Johnson, K.L., Greenwood, J.A., 1997. An adhesion map for the contact of elastic spheres. J. Colloid Interface Sci. 192 (2), 326–333.
Johnson, K.L., Greenwood, J.A., Higginson, J.G., 1985. The contact of elastic regular wavy surfaces. Int. J. Mech. Sci. 27 (6), 383–396.
Johnson, K.L., Kendall, K., Roberts, A.D., 1971. Surface energy and the contact of elastic solids. Proc. R. Soc. Lond. A 324, 1558.
Manners, W., Greenwood, J.A., 2006. Some observations on Persson's diffusion theory of elastic contact. Wear 261 (5), 600–610.
Maugis, D., 1992. Adhesion of spheres: the JKR-DMT transition using a Dugdale model. J. Colloid Interface Sci. 150 (1), 243–269.
Maugis, D., 2000. Contact, Adhesion and Rupture of Elastic Solids. Springer.
McCool, J.I., 1987. Relating profile instrument measurements to the functional performace of rough surfaces. ASME J. Tribol. 109, 264–270.
Nayak, P.R., 1971. Random process model of rough surfaces. J. Lubr. Technol. 93 (3), 398–407.
Pashley, M.D., 1984. Further consideration of the DMT model for elastic contact. Colloids Surfaces 12, 69–77.
Pastewka, L., Robbins, M.O., 2014. Contact between rough surfaces and a criterion for macroscopic adhesion. Proc. Natl. Acad. Sci. 111 (9), 3298–3303.
Persson, B.N.J., 2001. Theory of rubber friction and contact mechanics. J. Chem. Phys. 115, 3840–3861.
Persson, B.N.J., 2002. Adhesion between an elastic body and a randomly rough hard surface. Eur. Phys. J. E 8, 385–401.
Persson, B.N.J., 2014. On the fractal dimension of rough surfaces. Tribol. Lett. 54 (1), 99–106.
Persson, B.N.J., Albohr, O., Tartaglino, U., Volokitin, A.I., Tosatti, E., 2005. On the nature of surface roughness with application to contact mechanics, sealing, rubber friction and adhesion. J. Phys. 17, 1–62.
Persson, B.N., Scaraggi, M., 2014. Theory of adhesion: role of surface roughness. J. Chem. Phys. 141 (12), 124701.
Sayles, R.S., Thomas, T.R., 1978. Surface topography as a nonstationary random process. Nature 271 (5644), 431–434.
Sneddon, I., 1946. The distribution of stress in the neighbourhood of a crack in an elastic solid. Proc. Roy. Soc. A. 187 (1009), 229–260.
Tabor, D., 1977. Surface forces and surface interactions. J. Colloid Interface Sci. 58 (2).
Whitehouse, D.J., 2001. Fractal or fiction. Wear 249 (5–6), 345–353.
Xu, Y., Jackson, R.L., 2017. Statistical models of nearly complete elastic rough surface contact-comparison with numerical solutions. Tribol. Int. 105, 274–291.
Xu, Y., Jackson, R.L., Marghitu, D.B., 2014. Statistical model of nearly complete elastic rough surface contact. Int. J. Solids Struct. 51, 1075–1088.
Zhang, X., Xu, Y., Jackson, R.L., 2017. An analysis of generated fractal and measured rough surfaces in regards to their multi-scale structure and fractal dimension. Tribol. Int. 105, 94–101.